Geophysical Journal International

Observation and scaling of microearthquakes from the Taiwan Chelungpu-fault borehole seismometers

Yen-Yu Lin,[1] Kuo-Fong Ma[1] and Volker Oye[2]

[1]*Department of Earth Sciences and Institute of Geophysics, National Central University, Jhongli, Taiwan. E-mail: fong@earth.ncu.edu.tw*
[2]*NORSAR, Kjeller, Norway*

SUMMARY

Microearthquakes with magnitude down to 0.3 were detected by the Taiwan Chelungpu-fault Drilling Project Borehole Seismometers (TCDPBHS). Despite the large coseismic slip of 12 m at the drill site during the 1999 Chi–Chi earthquake, our studies show very little seismicity near the TCDPBHS drill site 6 yr after the Chi–Chi main shock. The microearthquakes clustered at a depth of 9–12 km, where the Chelungpu thrust fault turns from a 30° dipping into the horizontal decollement of the Taiwan fold-and-thrust tectonic structure. Continuous GPS surveys did not observe post-slip deformation at the larger slip region and no seismicity was observed near the drill site. Therefore we suggest that the thrust belt above the decollement is locked during this interseismic period. We further investigated source parameters of 242 microearthquakes by fitting ω^{-2}-shaped Brune source spectra to our observation data using a frequency-independent Q model. We find that the static stress drop increases significantly with increasing seismic moment. However, due to the intense debate on this topic of scaling-relations and the related self-similarity of earthquakes, we further improve the data analysis and correct for path and site effects using the Projected Landweber Deconvolution (PLD) method for events within some clusters. The PLD method analyses the source time functions of the larger and the smaller event by an iterative technique. As a result we received source dimensions and stress drops of larger events including path and site effect corrections. The results from the PLD method are less scattered and also show a positive relation between static stress drop and seismic moment. We find a similar positive trend for the apparent stress scaling with seismic moment.

Key words: Earthquake source observations; Seismicity and tectonics; Dynamics: seismotectonics.

GJI Seismology

1 INTRODUCTION

The Taiwan Chelungpu drilling project (TCDP) drilled a 2-km-deep hole (hole A) through the major slip zone at 1111 m of the 1999 Chi–Chi earthquake (M_w 7.6) in 2004. A seven-level vertical borehole seismic array (TCDPBHS) was installed in hole A covering the depth from 946 to 1274 m with 50–60-m depth intervals (Fig. 1) in 2006 July. For this layout, three seismometers were placed in the hanging wall and footwall, respectively. The forth one is located at the depth of 1110.28 m, close to the identified major slip zone (Ma *et al.* 2006) with coseismic slip of about 12 m. In addition, a surface short period seismic network with 10 stations was deployed in a radius of about 5 km around TCDP drill site between 2006 August and 2007 September, to better constrain microearthquake locations. Borehole installations with linear array configuration have been used to investigate seismically active fault zones (Daley & McEvilly 1990; Abercrombie 1995; Nishigami *et al.* 2001; Oye *et al.* 2004; Oye & Ellsworth 2005). Most of these studies, determined accurate

microearthquake locations by combining surface network and borehole array records and thereby identified the seismic activity within the fault zone (Jost *et al.* 1998; Tadokoro *et al.* 2000; Thurber *et al.* 2003; Ake *et al.* 2005). For events that are too small to be detected by surface networks, an alternative useful method is to use solely borehole stations and include information on polarization analysis in the inversion method (Abercrombie 1995; Oye & Roth 2003). In this study, we use observations of our near fault-zone TCDPBHS to investigate the seismic activity of a recently ruptured slip zone of the Chelungpu-fault and we try to draw some implications for the seismotectonics. In addition to that, source parameters such as magnitude, rupture dimension, stress drop, radiated energy and apparent stress were determined for these microearthquakes. Their results contribute to the compilation of earthquake scaling relationships and to the understanding of the dynamics of earthquakes.

The scaling relation of stress drop and apparent stress with seismic moment or earthquake size has been and still is debated in seismology. The scaling of static stress drop, which is defined as
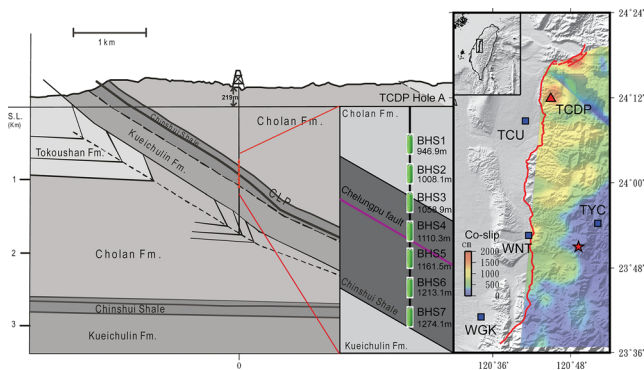
Figure 1. The layout of the TCDP borehole seismometer array is shown in the middle section, green rectangles. It is located (right section, red triangle), close to the surface trace of the Chelungpu-fault (red line) and in the region with largest coseismic slip of 12 m (Ji *et al.* 2001; colour scale in the map view). Red asterisk and red line indicate the Chi–Chi earthquake epicentre and the main surface rupture fault, respectively. Four short-period surface stations are showed in blue squares. The seven sensors are located in a depth from 946 to 1274 m with 50–60-m-depth intervals (middle section, Green rectangles). The number four sensor (BHS4) was installed very close to the Chelungpu main fault (middle section, purple line) inside the Chinshui Shale. The geological structures in this profile (Hung *et al.* 2007) are indicated on the figure.

the seismic moment divided by the cube of the source dimension (Eshelby 1957), provides the kinematic behaviour between small and large earthquakes. Apparent stress, which is proportional to the ratio of radiated energy and seismic moment, indicates the radiated energy released per unit fault area and unit slip. According to the energy budget of the earthquake process, a lower radiated energy release within a unit area would indicate that more energy is spent to create the fracture or is dissipated as heat and less energy is available to be radiated as seismic energy. The scaling in apparent stress to seismic moment indicates this dynamic property of earthquakes (Kanamori & Brodsky 2004). Several studies (Gibowicz *et al.* 1991; Kanamori *et al.* 1993; Singh & Ordaz 1994; Mayeda & Walter 1996; Mori *et al.* 2003; Ide *et al.* 2004; Oye *et al.* 2005; Yamada *et al.* 2007; Mayeda & Malagnini 2009) had made some effort in determination of the scaling relationship in either static stress drop or apparent stress to the seismic moment using different sets of data, especially borehole data from various regions to contribute to the observation of small earthquakes (Abercrombie 1995; Ide *et al.* 2003; Imanishi *et al.* 2004; Stork & Ito 2004; Venkataraman *et al.* 2006). The source parameters of earthquakes are often determined through the spectral analysis for an ω^{-2} model and a frequency-independent attenuation (Gibowicz *et al.* 1991; Kanamori *et al.* 1993; Singh & Ordaz 1994; Abercrombie 1995; Mayeda & Walter 1996; Stork & Ito 2004; Yamada *et al.* 2007). Abercrombie (1995) analysed the microearthquakes from deep borehole recordings at 2.5 km depth in the Cajon Pass, California and concluded that the significant positive relation in stress drop scaling and apparent stress increases with earthquake size for events smaller than *M* 3. However, Yamada *et al.* (2007) concluded constant stress drop and constant apparent stress scaling using spectral analysis for events of size *M* 0 to *M* 1 from African gold mine records. Another argument in this context is that the influence of attenuation is generally described by a constant, frequency-independent *Q*. This assumption is not always valid because *Q* may be frequency-dependent (Ide *et al.* 2003, 2004; Stork & Ito 2004; Oye *et al.* 2005) and might in particular have a strong influence on small events. Consequently, several studies suggested to use empirical Green's functions (eGf) to remove the influence of

path effects, such as attenuation in the spectral analysis (Ide *et al.* 2003, 2004; Mori *et al.* 2003; Oye *et al.* 2005; 2006; Venkataraman *et al.* 2006; Mayeda & Malagnini 2009). Ide *et al.* (2003) made a comparison between the standard spectral fitting approach and the eGf analysis using records from the Long Valley Exploratory Well at 2 km depth. They found that the positive trend of stress drop and apparent stress scaling turned into a constant, when using the eGf method. They also suggested that the spectral fitting analysis with frequency-independent *Q* may systematically underestimate the corner frequency and therefore an artificial positive trend might be obtained in the scaling-relations. However, Ide *et al.* (2004) also analysed aftershocks of western Tottori earthquakes and there they found a significant scaling of apparent stress with seismic moment. They suggested that complexities in the source model or frequency-bandwidth limitation might explain this scaling behaviour. Similarly, Abercrombie & Rice (2005) made an analysis of clusters from the Cajon Pass borehole records by spectral fitting and eGf methods. Both results show some tendency for increasing stress drop and increasing apparent stress with increasing moment. In a further study by Stork & Ito (2004), path effects were eliminated by a frequency-dependent *Q* assumption, though they still concluded with an increase in apparent stress with increasing moment. Some arguments are concerned with limitations in the bandwidth of seismic records as the concern of fmax of Hanks (1982), mainly due to a limited upper sampling rate. The seismic energy is calculated from the velocity spectra and because over 80 per cent of the total energy is carried by frequencies that are larger than the corner frequency, the energy is generally underestimated for small magnitude events with high corner frequencies (Ide & Beroza 2001). Therefore, not correcting for a potential loss of energy at the high frequencies may provide an artificial trend to the scaling relations (Boore 1986; Bona & Rovelli 1998; Singh & Ordaz 1994; Hough 1996). In view of all the debates over the issue on scaling of static stress drop and apparent stress to seismic moments, we contribute to this compilation with our observations from a 1.3-km-deep vertical borehole seismic array in the Taiwan Chelungpu-fault.

2 THE TCDP BOREHOLE SEISMOMETER AND OBSERVATIONS

The TCDPBHS is a seven-level vertical borehole seismic array covering the depth from 946 to 1274 m with 50–60-m-depth intervals (Fig. 1), which was installed in the zone of maximum coseismic slip mapped from the coseismic slip distribution of Ji *et al.* (2001) during the 1999 Chi–Chi earthquake in 2006 July. The sensors are velocity-type short period seismometers with Galperin deployment (IESE, NZ). The natural frequency of TCDPBHS sensors is near 4.5 Hz with the damping of about 29 per cent. The sensitivity approaches to the level of 1.6 V cm^{-1} s^{-1}. Since 2006 November, the deployment was successfully monitoring microearthquake activities near the Chelungpu-fault in continuous recording mode. From the start on the sampling rate was set to 1000 Hz and since 2008 January decreased to 200 Hz. The removal of instrument response, correction of the Galperin angle and the orientation of the three-component sensors were carried out systematically before the analysis of waveforms.

To assure the quality of the data, all continuous data of the first half year were investigated visually and events were classified into different groups. Events associated with downgoing waves along the vertical borehole geophones were considered to be human activity related and were therefore discarded. Events with clear *P* and
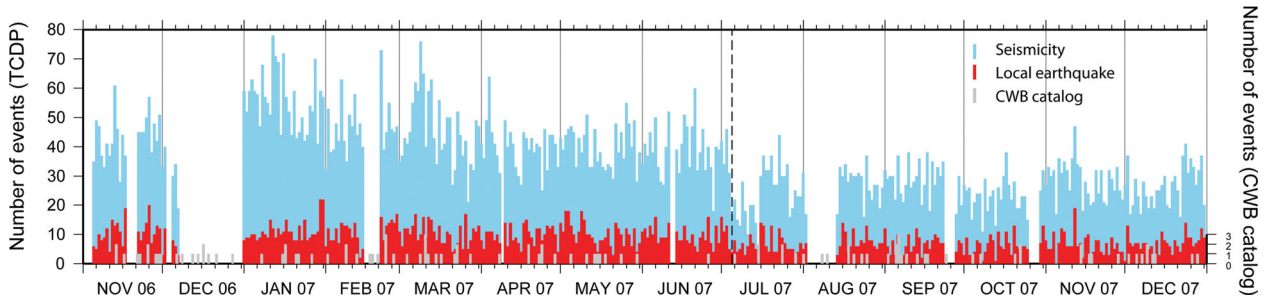
TCDP Seismicity (2006/11 ~ 2007/12)

Figure 2. Recorded seismicity by TCDPBHS from 2006 November to 2007 December. Blue bars show the background seismicity including regional earthquakes and teleseismic events. Red bars indicate local earthquakes with $\Delta t_{\rm sp} < 2$ s. Grey bars are events from Central Weather Bureau (CWB) catalogue recorded by surface stations (axis scale on the right). The blank areas of the blue and red bars are related to instrument malfunction. The dashed line at 2007 July 4 is the date when drill site construction. This correlates with higher noise levels and therefore lower detection capability of the regional seismicity. The detectability of the local seismicity does not seem to be affected.

S waves were further classified with respect to the mean traveltime difference between *S*- and *P*-wave arrivals ($\Delta t_{\rm sp}$). In this study, we focused on the events with the $\Delta t_{\rm sp}$ of less than 2.0 s to investigate the fault zone related events. After visual inspection of the first half year of continuous data, we developed semi-auto-picking techniques to increase the efficiency on the event identification. The semi-auto-picking technique considered the ratio of short-term average amplitudes (STA) and long-term average amplitudes (LTA) for *P*-phase picking. To confirm that upgoing waves are real microearthquakes, we calculated cross-correlation coefficients and delay times of *P* phases between the seven-level borehole seismometers. In the next step we picked the *S* wave manually to further select only events with $\Delta t_{\rm sp} < 2.0$ s. The comparison of the local events we obtained between the semi-auto-picking and the visualized picking for the first half a year data reached about 90 per cent accuracy.

During 14 months of continuous recording, 13 232 seismic events were classified, including regional and teleseismic events. Among them, 2780 events have $\Delta t_{\rm sp} < 2.0$ s and we call these from now on 'local events'. In average, about seven to eight local events were detected daily by the TCDPBHS. Fig. 2 shows the temporal distribution of the seismicity recorded by the TCDPBHS, indicating the events with $\Delta t_{\rm sp} < 2.0$ s. Due to the site construction, the noise level in high frequency increased after 2007 July 4, but with less influence to the identification of $\Delta t_{\rm sp} < 2.0$ s. Comparing the amount of microearthquakes detected by TCDPBHS and CWBSN, the result indicates that TCDPBHS has much lower detection threshold for microearthquakes in the volume of interest. This is mainly due to the low noise level in the borehole and absence of high attenuation in the uppermost few hundred meters of the crust. The site is also far away from human activities. Fig. 3 shows a histogram of events with $\Delta t_{\rm sp} < 6.0$ s, which indicates that a zone of high seismicity exists with $\Delta t_{\rm sp}$ 1.0–2.0 s. Only few events occurred with $\Delta t_{\rm sp}$ smaller than 1.0 s.

To examine the TCDPBHS capability, we made the synthetic signal-to-noise ratio (S/N) to the function of distance and magnitude to examine the detection limit of the TCDPBHS at the distance for a given magnitude. For a given magnitude, we constructed the corresponding velocity spectra by considering Brune's ω^{-2} model for a certain distance and t^*, where an attenuation factor, Q^S, of 166 (Wang *et al.* 2012) was considered. The maximum amplitudes of the obtained velocity spectra were then divided by the average noise level of TCDPBHS as of $5.24 \times$ E-6 cm s^{-1} to obtain the
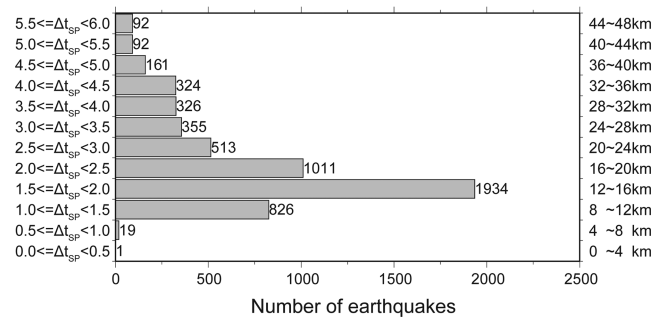
Earthquake Statistics

Figure 3. Earthquake statistics for $\Delta t_{\rm sp} < 6.0$ sec of TCDPBHS. Grey bars show number of events with 0.5 s of $\Delta t_{\rm sp}$ time interval showing on the left axis. The right axis indicates the associated hypocentre distance of the $\Delta t_{\rm sp}$ time with an average constant velocity (Kim *et al.* 2005), $Vp = 4.10$ km s^{-1} and $Vs = 2.60$ km s^{-1}.

synthetic S/N as function of distance to the magnitudes as shown in Fig. 4 curves. If we consider the S/N of 1.5 as the threshold for signal detection, the intersections of the S/N = 1.5 to the curves represented in Fig. 4 indicate the TCDPBHS detection capability to the distance and magnitude. However, since the synthetic S/N was made for a smooth spectrum curve, the capability we received could be considered as a lower bound of TCDPBHS capability. The result indicates that the limitation of microearthquake detection of TCDPBHS approaches $M_{\rm w}$ −0.5 for the events within the distance of 1km, which shows an improvement of the TCDPBHS to the magnitude completeness, $M_{\rm C}$, compared to the regular surface network of CWBSN with $M_{\rm C}$ of M 2.0 (Ma *et al.* 2005).

2.1 Microearthquake locations and seismicity in the Chelungpu-fault near the TCDPBHS

The locations of the local events were determined with a directed grid-search inversion similar to the method as described in Oye & Roth (2003). The input parameters for the inversion only consist of *S*–*P* arrival time measurements ($\Delta t_{\rm sp}$) and the direction of the incoming wavefield, that is, azimuth and incidence angles derived from *P*-wave polarization analysis. Using only traveltime

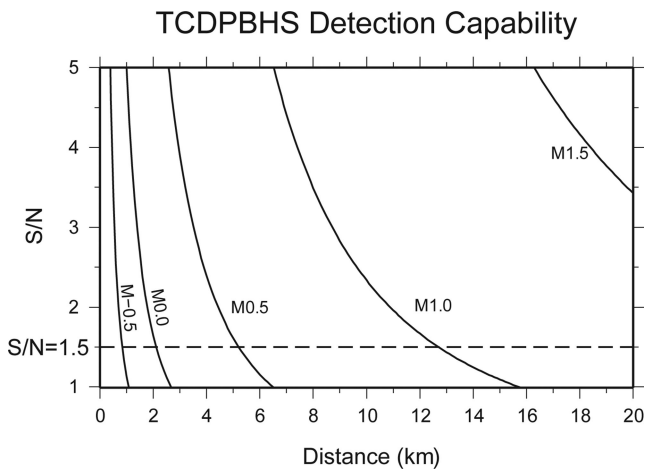## TCDPBHS Detection Capability

Figure 4. The TCDPBHS detection capability as function of distance and magnitude. The curves represent the synthetic S/N as function of distance for the given magnitudes and the dashed line indicates the constant for signal to noise (S/N) of 1.5, marked as single detection level of the TCDPBHS. The intersections of the curves to the S/N = 1.5 dashed line, thus, indicate the TCDPBHS detection capability as function of distance and magnitude.

differences instead of absolute traveltimes stabilizes the inversion method, which only inverts for the hypocentre location, whereas the origin time is derived from the location. Most of the events were too small to be detected by the surface stations and we therefore used only the TCDPBHS for hypocentre determination. Due to strong electric noise at BHS6 and BHS7, we only used the remaining five stations of the vertical array. The inversion iteratively applies the generalized matrix inversion location method so as to minimize the residual. We obtain the residuals by comparing the observation at all levels in the array with travel times and arrival angles calculated with homogenous velocity model as 4.10 and 2.60 km s^{-1} for P wave and S wave, respectively. This velocity structure was an average 3-D velocity model for this area of Taiwan (Kim *et al.* 2005). We adopted that homogenous velocity model because the location of the borehole stations avoids a shallow structure with very low seismic velocity and we do not expect large velocity variation with a few kilometres in our study area. Due to the geometry of the vertical array, the location accuracy is limited for events that are far away from the array and errors in location are mainly due to uncertainties in the azimuth and in the velocity model. We therefore compared the hypocentre locations of some larger events ($M \sim 1.5$) that are detected on the surface network using (1) the full network consisting of surface network and borehole network and (2) only the borehole network. The comparison between the determined locations shows that the difference is less than 2 km in horizontal and less than 1 km in vertical directions (please see Supporting Information).Due to the data quality, only 270 out of the 2780 local events were finally located. Most of the located events have S/N ratios of larger than 4. Fig. 5 shows the distribution of these events. It shows that most events were clustered in a flat horizontal zone at about 10 km depth. This zone has also been identified as a deformation zone where the 30° dipping Chelungpu thrust flattens to a decollement of the Taiwan fold and thrust tectonic structure (Wang *et al.* 2002; Hung *et al.* 2007; Wang *et al.* 2007). An interesting observation is that there was not any seismicity around TCDPBHS and near the Chelungpu main fault even after 6 yr of the occurrence of the 1999 Chi–Chi earthquake. This observation indicates first, the possible complete stress drop of the Chi–Chi earthquake, which left no stress for the occurrence of aftershocks and secondly the lock of the splay
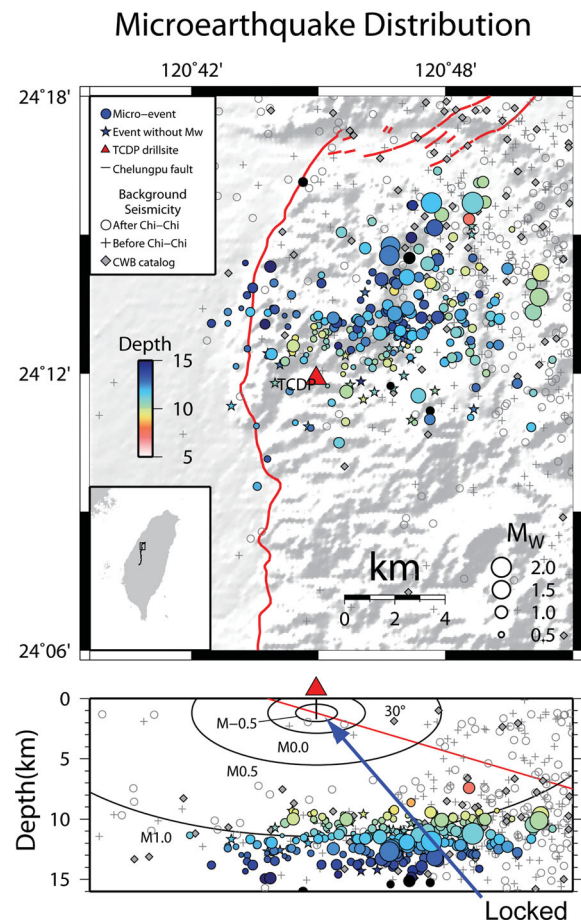
Microearthquake Distribution

Figure 5. The mircoearthquake distribution of TCDPBHS. Red triangle and red lines indicate location of TCDPBHS and the Chelungpu-fault, respectively. Solid circles show the events recorded from TCDPBHS. The colour scale and size indicate the depth of the events and magnitude, respectively. Solid asterisks are the events without magnitude scale. Crosses and open circles show the background seismicity before and after the Chi–Chi earthquake detected by CWBSN. Diamonds are the events recorded by CWBSN in the period of our analysis. Ellipses in the upper figure show the capability of TCDPBHS. Blue arrow points out the silent area of seismicity.

fault zone during the interseismic period. We further discuss this issue in Section 4.1.

The recording capability and the related detection threshold of the TCDPBHS are also shown in Fig. 5. It shows that within a region of 2 km from the TCDPBHS, any microearthquake larger than magnitude 0.0 should have been detectable. Since no such event was detected, it is likely that the main fault zone is silent and locked during this interseismic period.

2.2 Identification of event clusters using waveform cross-correlation

During the detecting procedures for event identification, we noted that several events are highly similar in waveforms. To quantify this observation, we performed waveform cross-correlation of the 2780 local events. We classified the events to be in the same cluster if their correlation coefficient is larger than 0.8 for the Z-component. We found 198 clusters, which have at least two events in each cluster. Fig. 6 shows the example for cluster number 13, which has five events showing similar waveforms. The first event,
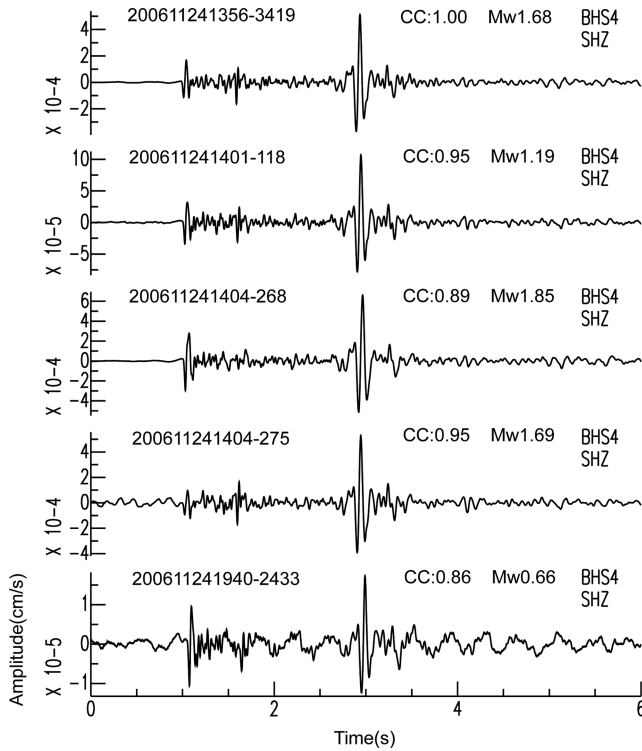
Figure 6. *Z*-component waveforms of BHS4 of the events in cluster number 13. Correlation coefficient, CC value and magnitude, M_w, are indicated on the figure for each event.

200611241356–3419, was selected as a template waveform. The correlation coefficients range from 0.86 to 0.95, suggesting very high waveform similarity. This high similarity indicates that those events have similar location and focal mechanism. We will further take advantage of these clusters to remove path and site effects during our investigation on source scaling relations.

3 SOURCE PARAMETER DETERMINATION OF MICROEARTHQUAKES

3.1 Estimation of the seismic moment, rupture dimension and stress drop

We determined the source parameters of the located microearthquakes to further determine the scaling of static stress drop and apparent stress with seismic moment. We estimated source parameters from the transverse components of 270 events by spectral analysis of Brune ω^{-2} model (Brune 1970) with an assumption of frequency-independent Q as below,

$$\Omega(f) = 2\pi f \Omega_0 \frac{f_C^2}{f_C^2 + f^2} \exp\left(\frac{-\pi f t}{Q}\right), \tag{1}$$

where t is traveltime, f is frequency and f_c is the corner frequency. We determined the spectral level Ω_0, Q and f_c of each microearthquake through a non-linear least-square fitting method (Marquardt 1963) (LSQENP) of the observed spectra of *Sh* wave simultaneously. The time-window for the analysis of the source spectra of *Sh* wave was fixed to 2 s (Fig. 7, middle figure, red bars) for all events to provide possible spectral fitting to 1 Hz in the low frequency part. We tested three window lengths in 2, 1 and 0.3 s

and obtained that the shortest cutting time-window length would produce an underestimation problem in corner frequency because of missing low frequency information in the spectral fitting processing. The window length should be longer than 1 s and we therefore considered 2 s as best time-window length. Besides, due to the limitation on S/N in the high frequency range, the spectral fitting was made from 1 Hz up to 50–70 Hz, where S/N ratio is larger than 1 (Fig. 7, bottom figure, blue bars). In this analysis, we used the records from BHS1 and BHS4 for the spectral analysis, because these two recordings are most stable in data quality. Other stations were often contaminated with strong coupling phases in the *S* wave or had strong electronic interferences, which mainly affected small events. Because the corner frequency is a source parameter that should be a constant for every individual event recorded at both stations, two steps in the LSQENP analysis were used for the source parameter determination. First, we obtained the values of Ω_0, Q and f_c by minimizing the residuals between the observed and the theoretical spectrum. Then, for every individual event, a corner frequency was obtained by averaging the value of the f_c recorded by both stations. Thus, the obtained f_c is fixed for the second step of the LSQENP, where we then estimate Ω_0 and Q. These two parameters were averaged for our further calculation with the fixed f_c. However, we discarded the events if differences in the f_c determination of BHS1 and BHS4 were larger than a 90 per cent confident interval in the statistic for all events. In total, 242 events fulfilled the quality criteria and were accepted for our source parameter determination.

The seismic moment of each event was calculated from Ω_0 using the relationship described by Brune (1970)

$$M_0 = \frac{4\pi \rho v^3 \Omega_0 d}{F}, \tag{2}$$

where ρ is the density (2700 kg m^{-3}), v is the seismic wave speed (2.60 km s^{-1} for *Sh* wave), d is the hypocentral distance and F is the radiation pattern. We consider an average radiation value of 0.63 for *Sh* waves (Aki & Richards 2002) and average the Ω_0 values of BHS1 and BHS4. The magnitudes of these 242 located microearthquakes determined from Ω_0, with magnitudes between M_w 0.33 and 2.20 (Fig. 5).

We further determined the rupture dimension and static stress drop of these events. The rupture dimension or the source radius r was determined from the corner frequency assuming the circular source model of Sato & Hirasawa (1973):

$$r = \frac{Cv}{2\pi f_c}, \tag{3}$$

where C is a constant (1.9 for *Sh* wave) (Stork & Ito 2004) and v is the seismic wave speed (2.60 km s^{-1} for *Sh* wave). The static stress drop, $\Delta\sigma_s$, is estimated from M_0 and r (Eshelby 1957).

$$\Delta\sigma_s = \frac{7M_0}{16r^3}, \tag{4}$$

The rupture dimension and stress drops of these events range from 21 to 204 m and 4.41E-4 to 2.40 MPa as listed in Table S1, respectively. Further discussion on the scaling of these parameters to the size of earthquakes will be addressed later in the discussion.

3.2 Estimation of the radiated energy and apparent stress

The radiated energy was obtained by integrating three component velocity seismograms (Ide *et al.* 2003)

$$E^c = 4\pi \rho v^c r^2 2 \int_{f_0}^{f_1} \left| \dot{u}(f) \exp\left(\frac{\pi f t}{Q^c}\right) \right|^2 df, \tag{5}$$
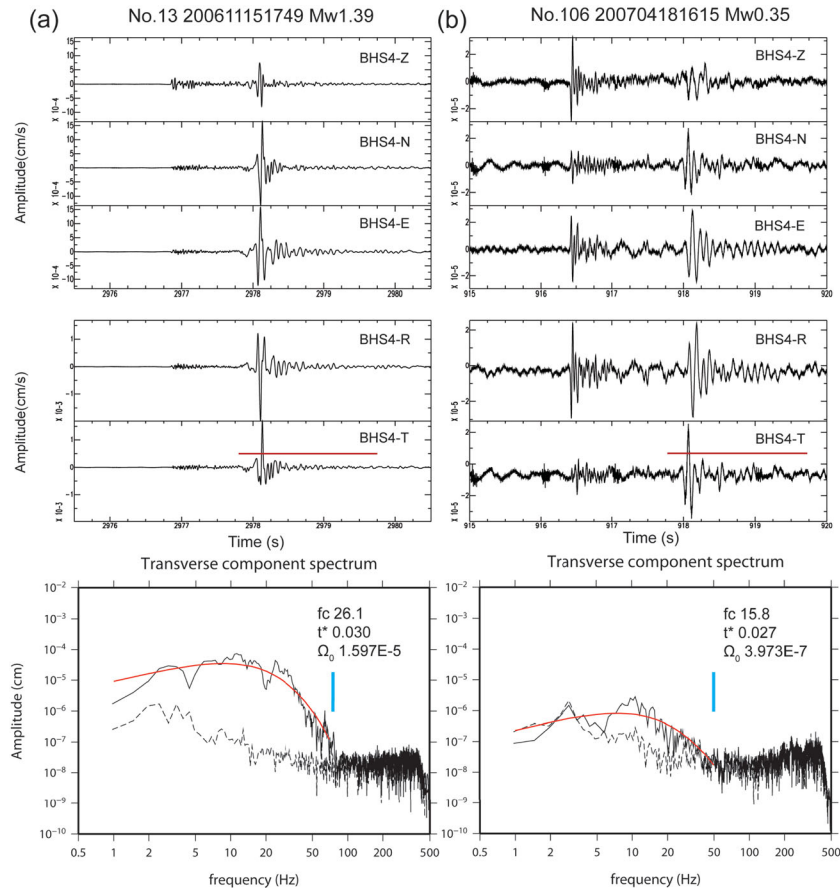
Figure 7. (a) and (b) show the *Z*, *N* and *E* component seismograms (top section), radial and transverse component seismograms (middle section) and spectrum in transverse component (bottom section) of event number 13, 200611151749 M_{w} 1.39 and number 106, 200704181615 M_{w} 0.35, respectively. Red lines in the middle section indicate the time-window we cut for spectral fitting. Red curves and dotted lines in the bottom section indicate best fitting curves and noise spectrum, respectively. Blue bars are the upper limit of fmax.

where *c* is the type of wave, *P* or *S* wave, ρ is the density (2700 kg m^{-3}), *v* is the velocity of *P* or *S* wave (4.10 and 2.60 km s^{-1} for *P* and *S* wave, respectively) and *r* is the distance from source to receiver. Q^P is a constant value about 220 from *Q* structure study in Taiwan (Wang *et al.* 2010) and Q^S is given from the best fitting parameter *Q* of the pervious spectral analysis. We applied energy corrections for frequency-bandwidth limitations following Ide & Beroza (2001). In our case, the average corner frequency of the events we determined is about 15.8 Hz and the available frequency bandwidth is 60 Hz for most of the events. By considering the correction provided by Ide & Beroza's (2001), we have increased the calculated radiated energy in average by 30 per cent to our determined total radiated energy. The total radiated energy (*E*) is the sum of E^P and E^S. The apparent stress, σ_{a}, is calculated from the total energy *E* and the seismic moments M_0 (Kanamori & Brodsky 2004)

$$\sigma_{\mathrm{a}} = \mu \frac{E}{M_0} = \frac{E}{\overline{D}S}, \tag{6}$$

where μ is the rigidity (1.8×10^4 MPa). The apparent stress represents the radiated energy released per unit area and unit slip on the fault zone and thus, the scaling of the apparent stress to different sizes of events indicates dynamic processes on the fault at different scales (Kanamori & Brodsky 2004). The apparent stresses of these events range from 5.88E-4 to 1.46 MPa, as also listed in Table S1.

4 DISCUSSION

4.1 Implications on seismotectonics from microearthquake distributions

The near horizontal distribution of microearthquakes from the flat deformed zone at about 10 km with no seismicity on the main rupture Chelungpu-fault observed from our TCDPBHS, show similar patterns as the distribution of the relocated aftershocks of the Chi–Chi earthquake (Chang *et al.* 2000; Carena *et al.* 2002; Chang *et al.* 2007). The detecting capability of the TCDPBHS, as we have shown earlier, suggested that the lack of seismicity on the northern portion of the Chelungpu-fault near the drill site is real. This observation provides two possible implications for the northern part of the Chelungpu-fault, where the largest coseismic slip of up to 12 m was found. (1) The complete stress drop of the asperity in the northern portion of the fault left not even stresses for the occurrence of aftershocks. (2) The fault is locked during this interseismic period. Wu (2009) analysed electric logs from TCDP and concluded that the azimuth of the maximum horizontal principal stress (S_{hmax}) rotated around 90° from the regional tectonic stress direction (N130°E) after the earthquake. The minimum horizontal principal stress (S_{hmin}) magnitude was almost equal to the maximum horizontal principal stress (S_{hmax}) after the Chi–Chi earthquake, suggesting a complete stress drop at the Chelungpu-fault in the Chi–Chi earthquake (Wu 2009). The complete stress drop indicated that the

cumulative stresses on the Chelungpu main fault zone before 1999 Chi–Chi earthquake were totally released by the large coseismic slip of the earthquake, thus, left little shear stress on the fault. The low shear stress on the fault explains why the lack of microearthquakes occurred on the Chelungpu-fault. The geodetic observation from inversion of the GPS data for the post-seismic slip and interseismic slip modelling on the Chelungpu-fault plane gave a coupling ratio of 1.0 in this area, suggesting the fault in this region was strongly locked (Hsu *et al.* 2009). Our observations of microearthquakes location with no seismicity on the main fault might provide the direct evidence to the locked of the fault.

A near-complete stress drop from a locked splayed fault for a large earthquake might have mechanical implication in tectonics for the coupling between the splayed fault and the near horizontal detachment. The depth of detachment at about 10 km in the northern part of the Chelungpu-fault was well determined from the massive amount of relocated aftershocks by several studies (Hirata *et al.* 2000; Carena *et al.* 2002; Chen *et al.* 2002). Hsu *et al.* (2003) and (2009) also suggested a decollement depth of 8–12 km beneath the Central Ranges by GPS data inversion. This high seismicity detachment may be associated with the decollement of the Taiwan fold-and-thrust tectonic structure (Yue *et al.* 2005). This detachment, as shown by Hsu *et al.* (2009), consists of low shear stresses of ∼2 MPa and a low effective friction of ∼0.01. The exceptionally low shear stress suggests the possible existence of fluid. The tomography study of Wu *et al.* (2007) suggested a high Vp/Vs zone at 9 km depth beneath the northern portion of the Chelungpu-fault and Chen & Chen (2002) analysed magnetotelluric (MT) data in the northern part of the Chelungpu-fault concluded that a low resistivity zone exists at 10 km depth beneath the northern portion of the Chelungpu-fault, indicating the possible existence of fluid in the detachment. In addition to that, as shown earlier, the seismicity in the detachment also occurs in earthquake clusters. The tectonic implication on the mechanics in the coupling of the locked splayed fault to the high seismicity with clusters of the horizontal detachment is an interesting subject to explore whether or not this locked splayed fault in the fold-and-thrust belt is a typical and a near complete stress drop will be always a consequence once the earthquake ruptured the splayed fault.

4.2 Scaling of rupture dimension and stress drop with frequency independent Q correction and with eGF correction

In Fig. 8(a), we show the determined corner frequencies and related source dimension and compare them against the seismic moment (corresponding to M_w of about 0 to 2). There is no obvious trend in the data, revealing more or less constant corner frequencies over the observed magnitude range. However, the scatter in the data is quite large and the source dimension seems to get larger and the scatter is smaller with increasing magnitude. The smallest observed source dimension reaches the value of about 20 m. Fig. 8(b) shows the relationship of the stress drop against the seismic moment for these microearthquakes. It shows an increase of the stress drop with increasing seismic moment. Alternatively, we tried to use a main fault plane (Strike = 15, Dip = 20, Rake = 110) to correct the radiation pattern more precisely, assuming that all microearthquakes would have a very similar source mechanism. This assumed main fault plane was determined by P wave first motion solution from an event (M 1.5) which is clearly recorded by the surface network. However, the slope of the alternatively determined regression line
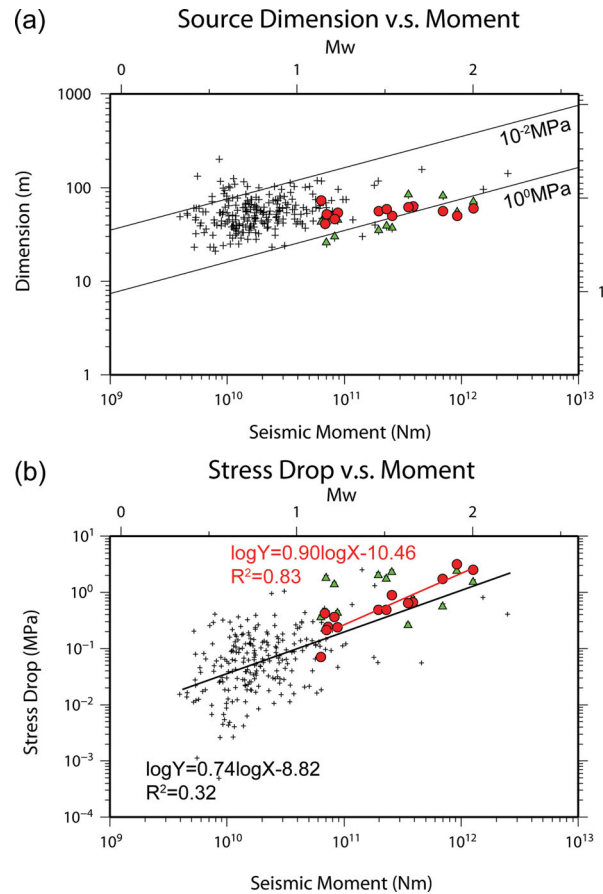
Figure 8. (a) Source dimension and seismic moment. Solid lines indicate constant stress drop. Black crosses show the results from spectral fitting analysis. Red circles are the results from PLD analysis. Green triangles indicate the results from spectral fitting analysis for the same events. (b) Stress drop and seismic moment. Red line is a regressive line from PLD analysis. Black line indicates a regressive line from spectral fitting analysis.

only differs by 10 per cent, revealing a similar relation and hence we further used the more conservative model of mean focal mechanism corrections. However, several investigations of source parameter determination of small events had shown the possible influence of frequency dependent Q, the trade-off between Q and corner frequency and frequency-bandwidth limitation of the data (Ide *et al.* 2003, 2004; Mori *et al.* 2003; Oye *et al.* 2005; Venkataraman *et al.* 2006; Mayeda & Malagnini 2009). For further scaling analysis we remove the path effect directly through the deconvolution.

We used the cluster events identified in Section 2.2 to analyse the scaling of source parameters with path effect correction by using an eGf method. In this study, an iterative technique of deconvolution, Project Landerweber Deconvolution (PLD), was used to calculate source time functions of the main event in each pair. Compared to the typical spectral division deconvolution technique, we can avoid the critical value division problem. The PLD is also more efficient in case of events with small difference in magnitudes (Lanza *et al.* 1999). The Landweber technique scheme is as follows (Bertero *et al.* 1997; Lanza *et al.* 1999),

$$f_{n+1} = f_n + \tau\, G^T * (u - G * f_n), \qquad (7)$$

where f is the relative source time function, n is the number of iterations, u indicates the main event waveform, G is the eGf, $G^T(t) = G(t)$, denotes the convolution product, τ is the relaxation operator.
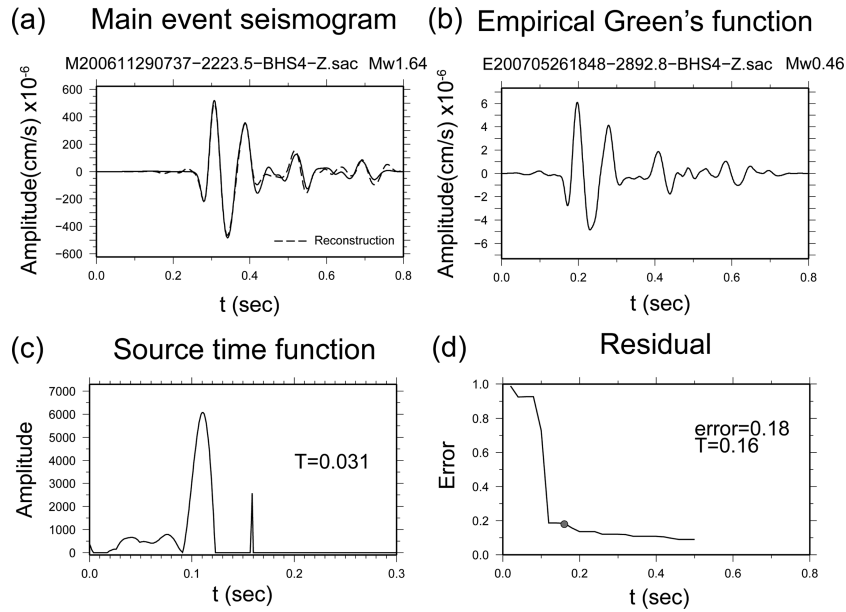
Figure 9. An example of the PLD analysis (a) Solid line and dotted line show the seismogram of main event and reconstructed event, respectively. (b) Empirical Green's function of the analysis (c) Black line is the source time function and *T* indicates the duration time of the source time function (d) Residual of the analysis. Grey dot indicates the time range of calculation ($t = 0.16$) and the residual (error = 0.18) in this analysis.

Table 1. Waveform similarity pairs used in this study: result of PLD analysis Source parameters estimation of 14 pairs for PLD analysis. In each pair, there are a main event and a smaller event used as an empirical Green's function. If more than two events were selected to be pairs from the same cluster, the smallest event was chosen as an empirical Green's function.

Number	Type	Date	Hour	Minutes	Seconds	Cluster #	M_w	Duration (s)	R-PLD (m)	Stress drop PLD (Mpa)	R Spectral (m)	Stress drop Spectral (MPa)
1	Main	2006/11/24	13	56	3419.9	13	1.66	0.035	63	6.65E − 01	60	7.73E − 01
	Empirical	2006/11/24	19	40	2433.9	13	0.66					
2	Main	2006/11/24	14	1	118.03	13	1.18	0.028	51	2.45E − 01	51	2.24E − 01
	Empirical	2006/11/24	19	40	2433.9	13	0.66					
3	Main	2006/11/24	14	4	268.49	13	1.83	0.031	56	1.73E + 00	82	5.61E − 01
	Empirical	2006/11/24	19	40	2433.9	13	0.66					
4	Main	2006/11/29	7	37	2223.5	15	1.64	0.031	62	6.50E − 01	84	2.60E − 01
	Empirical	2007/05/26	18	48	2892.8	15	0.46					
5	Main	2007/10/20	6	12	751.08	15	1.47	0.028	56	4.90E − 01	35	2.02E + 00
	Empirical	2007/05/26	18	48	2892.8	15	0.46					
6	Main	2007/10/20	6	33	1996.9	15	1.54	0.025	50	8.99E − 01	37	2.29E + 00
	Empirical	2007/05/26	18	48	2892.8	15	0.46					
7	Main	2007/01/14	12	34	2046.9	31	1.51	0.029	59	4.90E − 01	39	1.75E+00
	Empirical	2007/02/05	0	29	1786	31	0.41					
8	Main	2007/02/27	10	6	393.99	58	1.17	0.024	52	2.14E − 01	26	1.80E + 00
	Empirical	2007/02/27	19	51	3083.8	58	0.46					
9	Main	2007/03/09	21	52	3128.2	70	1.14	0.036	73	7.09E − 02	43	3.57E − 01
	Empirical	2007/03/09	21	51	3080	70	0.57					
10	Main	2007/08/16	10	47	2823	153	2.01	0.03	60	2.54E + 00	71	1.53E + 00
	Empirical	2007/08/15	15	46	2809.1	153	1.19					
11	Main	2007/08/16	10	59	3547.5	153	1.91	0.025	50	3.18E + 00	55	2.40E + 00
	Empirical	2007/08/15	15	46	2809.1	153	1.19					
12	Main	2007/09/20	11	26	1607.3	169	1.23	0.03	54	2.39E − 01	45	4.28E − 01
	Empirical	2007/09/21	12	37	2238.1	169	0.41					
13	Main	2007/09/23	13	40	2414.4	172	1.21	0.021	46	3.65E − 01	30	1.38E + 00
	Empirical	2007/09/23	21	41	2483.9	172	0.45					
14	Main	2007/11/24	6	46	2777	187	1.16	0.023	41	4.21E − 01	51	2.26E−01
	Empirical	2007/11/24	15	0	8.061	187	0.44					

If $\|u - G \times f_n\|$ approaches a minimum after a specified number of iterations, we can obtain the source time function of the main event. The residual is calculated as follows

$$\varepsilon = \left[\sum_{i=1}^{N} [A_{\text{obs}}(i) - A_{\text{rec}}(i)]^2 \Big/ \sum_{i=1}^{N} [A_{\text{obs}}(i)]^2 \right]^{\frac{1}{2}}, \quad (8)$$

where N is the number of time points, $A_{\text{obs}}(i)$ is the main event seismogram equal to u and $A_{\text{rec}}(i)$ is the reconstructed seismogram equal to $G \times f_n$. We suggested that the residual must be less than 0.3 to ensure the waveform coherence between A_{obs} and A_{rec} in this experiment. Fig. 9 shows an example of the PLD analysis. The reconstructed seismogram, A_{rec} (Fig. 9a dot line), is very consistent to the seismogram of the main event, A_{obs} (Fig. 9a solid line). The duration time, manually estimated from the source time function is 0.031 s in Fig. 9(c).

We selected 14 pairs or events from 9 clusters where the magnitude difference between the events is at least equal to or greater than 0.5 for the PLD analysis (Table 1). If more than two events were selected to be pairs within the same cluster, the smallest event was chosen to be the eGf of the larger events. We determined the duration of the source time function of the larger earthquakes, $\tau_{s,}$ through the PLD to determine the source dimension, L, following (Lanza *et al.* 1999):

$$L = \frac{\tau_S \upsilon}{1 + \upsilon \sin \theta / c(s)}, \quad (9)$$

where υ is the rupture velocity, which is now considered to be 0.75 times the S-wave velocity, $c(s)$ is the velocity at the source region and θ is the angle between the normal to the fault plane and the outgoing ray. Here we assumed a horizontal fault plane, thus, θ is the angle of the outgoing ray to the station. In the analysis we used the Vp and Vs velocities at the depth of about 11 km as determined by Kim *et al.* (2005). Figs 8(a) and (b) show also the scaling relationship of the source dimension and stress drop to the seismic moments using the PLD method for Q correction, respectively, in comparison to the relationship with frequency-independent Q correction. The results after the Q correction from the PLD method show that the determined rupture dimensions are more distinctively constant within the observed ranges of magnitudes (Fig. 8a) and the stress drop is increasing (Fig. 8b) with the seismic moment.

4.3 Scaling of radiated energy and apparent stress to the seismic moments

Figs 10(a) and (b) show the relationship of the radiated energy and the apparent stress to the seismic moment, respectively. In this radiated energy study, we only use the spectral fitting analysis without using eGf analysis due to the noise in high frequencies (>50 Hz), which is preventing us from determining the corner frequency of our small eGf events in our clusters. The range of apparent stresses determined is between 10^{-3} and 1 MPa and indicates an increasing relation to the seismic moment. For the estimation of the energy radiation from P and S waves, our results show that the energy from the S wave is about 20 times larger than the P-wave energy (Fig. 11). It indicates that the radiated energy of P wave is about 5 per cent of total seismically radiated energy. This result is similar to the result of Abercrombie (1995), that 7 per cent P-wave energy radiation of total radiated energy.

We compared our results to other studies and split them into two groups: one group that uses spectral fitting or similar analysis (Gibowicz *et al.* 1991; Kanamori *et al.* 1993; Singh & Ordaz 1994; Abercrombie 1995; Mayeda & Walter 1996; Stork & Ito 2004;
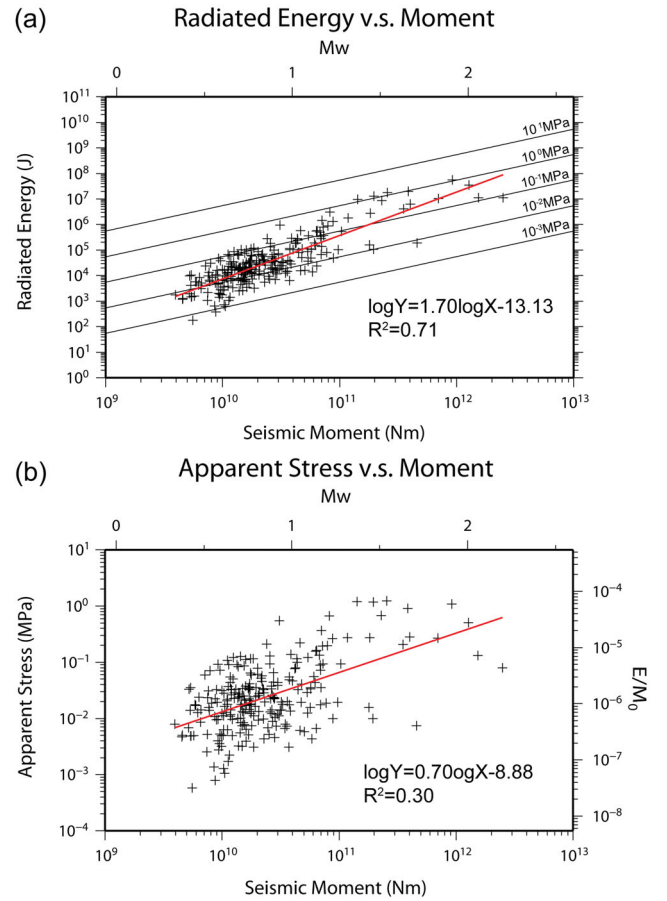

Figure 10. (a) Radiated energy and seismic moment. Black crosses indicate the data points. Red line is a regressive line. Black lines show constant apparent stress. (b) Apparent stress and seismic moment. Red line is a regressive line.

Yamada *et al.* 2007) and another group that uses eGf analysis (Ide *et al.* 2003, 2004; Mori *et al.* 2003; Oye *et al.* 2005; Venkataraman *et al.* 2006; Mayeda & Malagnini 2009), as shown in Fig. 12. Many of these studies investigated events of similar size as ours of about M_w 0.0–2.5. This study's results show similar patterns as the results from Stork & Ito (2004) and from Abercrombie (1995), that is, an increase of apparent stress with seismic moment with scatter around 10^{-3}–10 MPa.

Fig. 12 shows that, except for the study of Yamada *et al.* (2007), most of the studies using spectral fitting analysis and other methods show an increasing relation of the apparent stress to the seismic moments, with scattering mostly in the range of 10^{-2}–10 MPa. Similar feature is also found for the South African mine borehole data set of Gibowicz *et al.* (1991), even though their event magnitudes reach down to -4 to -2. The results from eGf analysis tends to narrow the scattering and suggest near constant values in apparent stress in the range of 10^{-2}–10 MPa, except the data set by Oye *et al.* (2005), where the events from a deep ore mine have apparent stresses of between 10^{-1} and 10^{-3} MPa. In our study, we could unfortunately not carry out the eGf analysis due to limited resolution in high frequencies in our data. However, either the increasing relation is an apparent relationship due to the instrumentation limitation or an indication in the difference of scaled energy in various sizes of earthquakes, our TCDPBHS data is another set of important data to this debate.
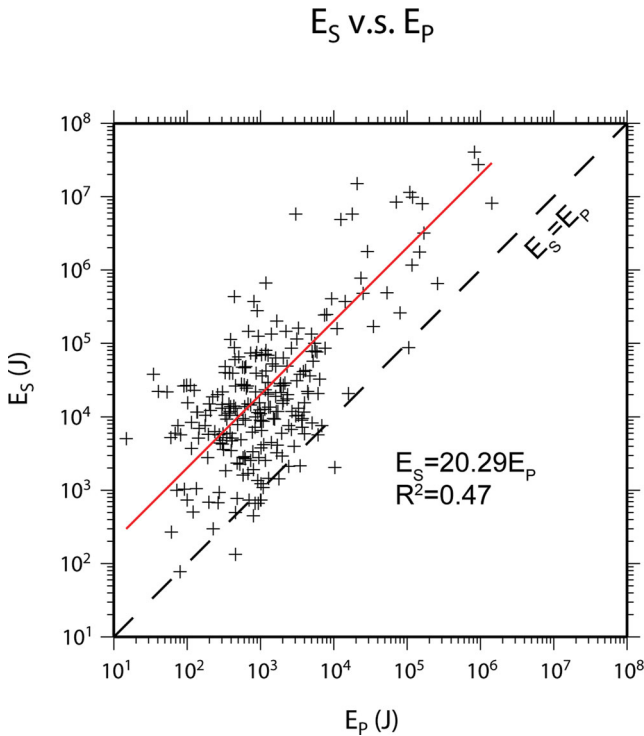
E_S v.s. E_P

Figure 11. Comparison of radiated energy in *P* and *S* waves. Red line indicates a regression. Dotted line shows the line of E_P equal to E_S.

5 CONCLUSION

The TCDP borehole seismometers array, which was a vertical array deployed through a recent large slipped fault zone of the 1999 Chi–Chi (M_w 7.3) earthquake, is a unique setting in the world. We monitored microearthquake activity down to magnitude 0.0 for the region surrounding this large coseismic slip zone 6 yr after the earthquake. Considering the TCDPBHS recording capability, we confirm

that no seismic activity occurred on the coseismic slip fault zone during the observation period, which also gives a good agreement to GPS observation as no post-slip was observed in the large coseismic zone. These observations suggest that the Chelungpu-fault is locked during this interseismic period. The Chelungpu-fault is considered as a splayed fault from the fold-and-thrust tectonic setting of Taiwan and the complete absence of microseismicity near the TCDP is also an indication for a complete stress drop during the main shock. Most of the microearthquakes that we detected occurred at a 10-km-deep flat zone, a western extension of the decollement. This flat deformed zone appeared to have repeating clusters of microearthquakes, which might be related to fluid pressurization. This observation suggests the lock of a splayed fault with active cluster type seismicity from the decollement related deformed zone. Whether or not this seismotectonic model is a general feature for other regions with similar tectonic settings or, only a feature for the Chelungpu-fault, requires further observations in different regions and possibly from fault zone dynamic modelling.

In addition to the seismotectonic implication of our observation, our kinematic source parameter scaling analysis suggests an increase of stress drop with seismic moment between magnitudes 0 and 2. To reduce the influence of path effects (*Q* effect), we also estimated the source parameters by eGf using the PLD method. The investigation still results in a positive relationship, but with less scattering. For dynamic parameter scaling, the relation between apparent stress and seismic moment were made, which also showed positive relationship, indicating different dynamic behaviour in magnitudes of 0 to 2. When we compare our results with a wider range of magnitudes (*M* −4 to 8), our observations of apparent stresses cluster in the range between 10^{-3} and 1 MPa, similarly to other observations. Thus, our observation seems not to have the ability to discriminate the debate on the constant or positive relationship of the apparent stress (scaled energy) to the seismic moment. However, our TCDPBHS is another data set to give the contribution of the global compilation on the investigation of the source scaling for microearthquakes.
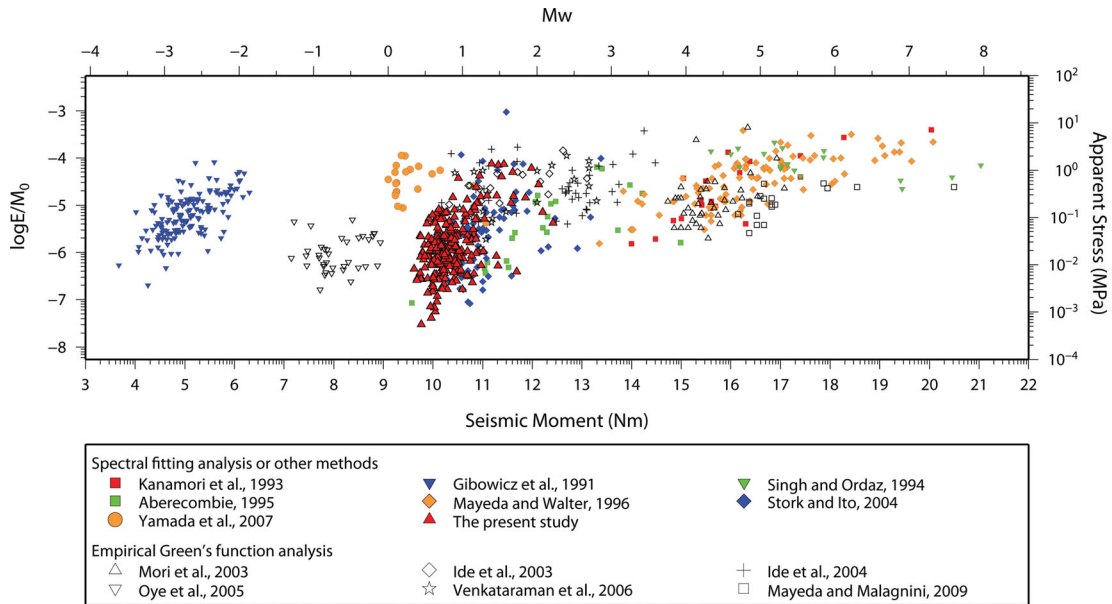

Figure 12. Composition of several previous studies on apparent stress scaling, covering a large range of magnitudes. Colour symbols show the results analysing by spectral fitting method or other method. Red triangles indicate the results of this study.

REFERENCES

Abercrombie, R.E., 1995. Earthquake source scaling relationships from -1 to 5 M_L using seismograms recorded at 2.5-km depth, *J. geophys. Res.,* **100**(12), 24015–24036.

Abercrombie, R.E. & Rice, J.R., 2005. Can observations of earthquake scaling constrain slip weakening?, *Geophys. J. Int.,* **162**, 406–424.

Ake, J., Mahrer, K., O'Connel, D. & Block, L., 2005. Deep-Injection and Closely Monitored Induced Seismicity at Paradox Valley, Colorado, *Bull. seism. Soc. Am.,* **95**(2), 664–683.

Aki, K. & Richards, P., 2002. *Quantitative Seismology,* University Science Books, Sausalito, CA.

Bertero, M., Bindi, D., Boccacci, P., Cattaneo, M., Eva, C. & Lamza, V., 1997. Application of the projected Landweber method to the estimation of the source time function in seismology, *Inversion Problems,* **13**, 465–486.

Bona, M.D. & Rovelli, A., 1988. Effects of the bandwidth limitation on stress drops estimated from integrals of the ground motion, *Bull. seism. Soc. Am.,* **78**, 1818–1825.

Boore, D.M., 1986. The effect of finite bandwidth on seismic scaling relationships, in *Earthquake Source Mechanics,* Geophys. Monogr. Ser. 37, pp. 275–283, eds Das, S., Boatwright, J. & Scholz, C., American Geophysical Union, Washington, DC.

Brune, J., 1970. Tectonic stress and the spectra of seismic shear waves from earthquakes, *J. geophys. Res.,* **75**(26), 4997–5009.

Carena, S., Suppe, J. & Kao, H., 2002. Active detachment of Taiwan illuminated by small earthquakes and its control of first-order topography, *Geology,* **30**(10), 935–938.

Chang, C., Wu, Y., Shin, T. & Wang, C., 2000. Relocation of the 1999 Chi-Chi Earthquake in Taiwan, *Terr. Atmos. Ocean. Sci.,* **11**(3), 581–590.

Chang, C., Wu, Y., Zhao, L. & Wu, F., 2007. Aftershocks of the 1999 Chi-Chi, Taiwan, Earthquake: the first hour, *Bull. seism. Soc. Am.,* **97**(4), 1245–1258.

Chen, C. & Chen, C., 2002. Sanyi-Puli conductivity anomaly in NW Taiwan and its implication for the tectonics of the 1999 Chi-Chi, Taiwan, earthquake, *Geophys. Res. Lett.,* **29**(8), 1116–1118.

Chen, K., Huang, B., Wang, J. & Yen, H., 2002. Conjugate thrust faulting associated with the 1999 Chi-Chi Taiwan earthquake sequence, *Geophys. Res. Lett.,* **29**(8), 1277–1280.

Daley, T.M. & McEvilly, T.V., 1990. Shear-wave anisotropy in the Parkfield Varian well VSP, *Bull. seism. Soc. Am.,* **80**, 857–869.

Eshelby, J.D., 1957. The determination of the elastic held of an ellipsoidal inclusion and related problems, *Proc. R. Soc. Lond.,* **241**, 376–396.

Gibowicz, S.J., Young, R.P., Talebi, S. & Rawlence, D.J., 1991. Source parameters of seismic events at the underground research laboratory in Manitoba, Canada: scaling relations for events with moment magnitude smaller than -2, *Bull. seism. Soc. Am.,* **81**(4), 1157–1182.

Hanks, T.C., 1982. fmax, *Bull. seism. Soc. Am.,* **72**(6), 1867–1879.

Hirata, N., Sakai, S., Liaw, Z., Tsia, Y. & Yu, S., 2000. Aftershock observations of the 1999 Chi-Chi, Taiwan earthquake, *Bull. Earthq. Res. Inst. Tokyo Univ.,* **75**, 33–46.

Hough, S.E., 1996. Observational constraints on earthquake source scaling: understanding the limits in resolution, *Tectonophysics,* **261**, 83–96.

Hsu, Y., Simons, M., Yu, S., Kuo, L. & Chen, H., 2003. A two-dimensional dislocation model for interseismic deformation of the Taiwan mountain belt, *Earth planet. Sci. Lett.,* **211**, 287–294.

Hsu, Y., Avouac, J., Yu, S., Chang, C., Wu, Y. & Woessner, J., 2009. Spatiotemporal slip, and stress level on the faults within the western foothills of Taiwan: implications for fault frictional properties, *Pure appl. Geophys.,* **166**, 1853–1884.

Hung, J., Wu, Y., Yeh, E., Wu, J., TCDP scientific party, 2007. Subsurface structure, physical properties and fault zone characteristics in the scientific drill holes of Taiwan Chelungpu-fault drilling project, *Terr. Atmos. Ocean. Sci.,* **18**(2), 271–293.

Ide, S. & Beroza, G.C., 2001. Does apparent stress vary with earthquake size?, *Geophys. Res. Lett.,* **28**(17), 3349–3352.

Ide, S., Beroza, G.C., Prejean, S.G. & Ellsworth, W.L., 2003. Apparent break in earthquake scaling due to path and site effects on deep borehole recordings, *J. geophys. Res.,* **108**(5), 2271–2284.

Ide, S., Matsubara, M. & Obara, K., 2004. Exploitation of high-sampling Hi-net data to study seismic energy scaling: the aftershocks of the 2000 western Tottori, Japan, earthquake, *Earth Planets Space,* **56**, 859–871.

Imanishi, K., Ellsworth, W.L. & Prejean, S.G., 2004. Earthquake source parameters determined by the SAFOD Pilot Hole seismic array, *Geophys. Res. Lett.,* **31**, L12S09, doi:10.1029/2004GL019420.

Jost, M.L., Bubelberg, T., Jost, O. & Harjes, H.P., 1998. Source parameters of injection-induced microearthquakes at 9 km depth at the KTB Deep drilling site, Germany, *Bull. seism. Soc. Am.,* **88**(3), 815–832.

Ji, C., Helmberger, D.V., Song, T.A., Ma, K. & Wald, D.J., 2001. Slip distribution and tectonic implication of the 1999 Chi-Chi, Taiwan, earthquake, *Geophys. Res. Lett.,* **28**(23), 4379–4382.

Kanamori, H., Mori, J., Haukasson, E., Heaton, T.H., Hutton, L.K. & Jones, L.M., 1993. Determination of earthquake energy release and M_L using TERRASCOPE, *Bull. seism. Soc. Am.,* **83**(2), 330–346.

Kanamori, H. & Brodsky, E.E., 2004. The physics of earthquake, *Rep. Prog. Phys.,* **67**, 1429–1496.

Kim, K., Chiu, J., Pujol, J., Chen, K., Huang, B., Yeh, Y. & Shen, P., 2005. Three-dimensional V_P and V_S structural models associated with the active subduction and collision tectonics in the Taiwan region, *Geophys. J. Int.,* **162**, 204–220.

Lanza, V., Spallarossa, D., Cattaneo, M., Bindi, D. & Augliera, P., 1999. Source parameters of small events using constrained deconvolution with empirical Green's functions, *Geophys. J. Int.,* **137**, 651–662.

Ma, K., Chan, C. & Stein, R.S., 2005. Response of seismicity to Coulomb stress triggers and shadows of the 1999 Mw = 7.6 Chi-Chi, Taiwan, earthquake, *J. geophys. Res.,* **110**, B05S19, doi:10.1029/2004JB003389.

Ma, K. *et al*., 2006. Slip zone and energetics of a large earthquake from the Taiwan Chelungpu-fault Drilling Project, *Nature,* **444**, 473–476.

Marquardt, D., 1963. An algorithm for least-squares estimation of nonlinear parameters, *J. Soc. Ind. appl. Math,* **11**(2), 431–441.

Mayeda, K. & Walter, W., 1996. Moment, energy, stress drop and source spectra of western United States earthquakes from regional coda envelopes, *J. geophys. Res.,* **101**(5), 11195–11208.

Mayeda, K. & Malagnini, L., 2009. Apparent stress and corner frequency variations in the 1999 Taiwan (Chi-Chi) sequence: evidence for a step-wise increase at Mw ∼ 5.5, *Geophys. Res. Lett.,* **36**, L10308, doi:10.1029/2009GL037421.

Mori, J., Abercrombie, R.E. & Kanamori, H., 2003. Stress drops and radiated energies of aftershocks of the 1994 Northrigde, California, earthquake, *J. geophys. Res.,* **108**(11), 2545–2557.

Nishigami, K., Ando, M. & Tadokoro, K., 2001. Seismic observation in the DPRI 1800m borehole drilled into the Nojima fault zone, south-west Japan, *Island Arc,* **10**, 288–295.

Oye, V. & Roth, M., 2003. Automated seismic event location for hydrocarbon reservoirs, *Comput. Geosci.,* **29**, 851–863.

Oye, V., Chavarria, J.A. & Malin, P.E., 2004. Determining SAFOD area microearthquake locations solely with the Pilot Hole seismic array data, *Geophys. Res. Lett.,* **31**, L12S10, doi:10.1029/2003GL019403.

Oye, V., Bungum, H. & Roth, M., 2005. Source parameters and scaling relations for mining-related seismicity within the Pyhasalmi Ore Mine, Finland, *Bull. seism. Soc. Am.,* **95**(3), 1011–1026.

Oye, V. & Ellsworth, W.L., 2005. Orientation of three-component geophones in the San Andreas Observatory at Depth Pilot Hole, Parkfield, California, *Bull. seism. Soc. Am.,* **95**(2), 751–758.

Oye, V., Roth, M. & Bungum, H., 2006. Source parameters determined from microearthquakes in an underground ore mine, in *Earthquake Radiated Energy and the Physics of Faulting,* Geophys. Monogr. Ser. 170. pp. 75–80, eds Abercrembie, R.E., McGarr, A., Toro, G. & Kanamori, H., American Geophysical Union, Washington, DC.

Sato, T. & Hirasawa, T., 1973. Body wave spectra from propagating shear cracks, *J. Phys. Earth,* **21,** 415–431.

Singh, S.K. & Ordaz, M., 1994. Seismic energy release in Mexican subduction zone earthquakes, *Bull. seism. Soc. Am.,* **84**(5), 1533–1550.

Stork, A.L. & Ito, H., 2004. Source parameter scaling for small earthquakes observed at the western Nagano 800-m-deep Borehole, central Japan, *Bull. seism. Soc. Am.,* **94**(5), 1781–1794.

Tadokoro, K., Ando, M. & Nishigami, K., 2000. Induced earthquakes accompanying the water injection experiment at the Nojima fault zone, Japan: seismicity and its migration, *J. geophys. Res,* **105**(3), 6089–6104.

Thurber, C., Roecker, S., Roberts, K., Gold, M., Powell, L. & Rittger, K., 2003. Earthquake locations and three-dimensional fault zone structure along the creeping section of the San Andreas fault near Parkfield, CA: preparing for SAFOD, *Geophys. Res. Lett.,* **30**(3), 1112–1115.

Venkataraman, A., Beroza, G.C., Ide, S., Imanishi, K., Ito, H. & Iio, Y., 2006. Measurements of spectral similarity for microearthquakes in western Nagano, Japan, *J. geophys. Res.,* **111,** B03303, doi:10.1029/2005JB003834.

Wang, C., Tanaka, H., Chow, J., Chen, C. & Hong, J., 2002. Shallow reflection seismics aiding geological drilling into the Chelungpu fault after the 1999 Chi-Chi earthquake, Taiwan, *Terr. Atmos. Ocean. Sci.,* **13**(2), 153–171.

Wang, C., Lee, C., Wu, M. & Ger, M., 2007. Investigating the TCDP drill site using deep and shallow reflection seismics, *Terr. Atmos. Ocean. Sci.,* **18**(2), 129–141.

Wang, Y., Ma, K., Mouthereau, F. & Eberhart-Phillips, D., 2010. Three dimensional Qp- Qs-Tomography beneath Taiwan Orogenic Belt: comparison to the Tectonic and the Thermal Structure, *Geophys. J. Int.,* **180,** 891–910.

Wang, Y., Lin, Y., Ma, K. & Lee, M., 2012. Fault zone Q values derived from Taiwan Chelungpu Fault borehole seismometers (TCDPBHS), *Tectonophysics,* in press, doi:10.1016/j.tecto.2011.12.027.

Wu, Y., Chang, C., Zhao, L., Shyu, J.B.H., Chen, Y., Sieh, K. & Avouac, J., 2007. Seismic tomorgraphy of Taiwan: improved constraints from a dense network of strong motion stations, *J. geophys. Res.,* **112,** B08312, doi:10.1029/2007JB004938.

Wu, H., 2009. Physical properties and modeling stress heterogeneity in Chelungpu fault vicinity Dakeng, Taiwan, *PhD thesis*, National Central University, Taiwan.

Yamada, T., Mori, J., Ide, S., Abercrombie, R.E., Kawakata, H., Nakatani, M., Iio, Y. & Ogasawara, H., 2007. Stress drops and radiated seismic energies of microearthquakes in a South African gold mine, *J. geophys. Res.,* **112,** B03305, doi:10.1029/2006JB00453.

Yue, L., Suppe, J. & Hung, J., 2005. Structural geology of a classic thrust belt earthquake: the 1999 Chi-Chi earthquake Taiwan (Mw = 7.6), *J. Struct. Geol.,* **27**(11), 2058–2083.

SUPPORTING INFORMATION

Additional Supporting Information may be found in the online version of this article:

Figure S1. A surface network including nine surface stations was deployed around drilling site from November 2006 to September 2007. However, most of the events were too small to be recorded by the surface stations. Only three events (M_w ~1.5) in 2006 November were recorded by the surface stations, which could be used for earthquake locations. The comparison of the locations with and without surface stations is shown here. Solid circles mark the microearthquake locations with surface stations, while asterisks mark those without surface stations, for events 20061112–2136, 20061115–1749 and 20061129–0737 marked as number 1–3, respectively. The dotted lines represented the corresponding difference in locations. Grey squares show the locations of the surface stations and the red triangle is the TCDP borehole station. It shows that the differences in horizontal and vertical in location are close to 2 and 1 km, respectively.

Table S1. The catalogue of earthquakes analysed for the spectral fitting analysis. Source parameter estimations of 270 events by spectral fitting analysis. Symbols '-' indicate the events which cannot fit observed spectrum correctly or the difference in the f_c determinations of BHS1 and BHS4 beyond the 90 per cent confident interval in the statistic of all the events.

Please note: Wiley-Blackwell are not responsible for the content or functionality of any supporting materials supplied by the authors. Any queries (other than missing material) should be directed to the corresponding author for the article.